# Direct Atomic-Scale Imaging of Hydrogen and Oxygen Interstitials in Pure Niobium Using Atom-Probe Tomography and Aberration-Corrected Scanning Transmission Electron Microscopy

Yoon-Jun Kim,[†] Runzhe Tao,[‡] Robert F. Klie,[‡] and David N. Seidman[†,§,*]

[†]Department of Materials Science and Engineering, Northwestern University, Evanston, Illinois 60208, United States , [‡]Department of Physics, University of Illinois at Chicago, Chicago, Illinois 60607, United States , and [§]Northwestern University Center for Atom Probe Tomography (NUCAPT), 2220 Campus Drive, Evanston, Illinois 60208, United States. Author contributions: Y.J.K. prepared both TEM and APT samples and carried out APT measurements. R.T. performed the TEM/EELS experiments. Y.J.K., D.N.S., R.T., and R.F.K. analyzed the results and wrote and edited the manuscript.

ABSTRACT Imaging the three-dimensional atomic-scale structure of complex interfaces has been the goal of many recent studies, due to its importance to technologically relevant areas. Combining atom-probe tomography and aberration-corrected scanning transmission electron microscopy (STEM), we present an atomic-scale study of ultrathin ($\sim$5 nm) native oxide layers on niobium (Nb) and the formation of ordered niobium hydride phases near the oxide/Nb interface. Nb, an elemental type-II superconductor with the highest critical temperature (T_c = 9.2 K), is the preferred material for superconducting radio frequency (SRF) cavities in next-generation particle accelerators. Nb exhibits high solubilities for oxygen and hydrogen, especially within the RF-field penetration depth, which is believed to result in SRF quality factor losses. STEM imaging and electron energy-loss spectroscopy followed by ultraviolet laser-assisted local-electrode atom-probe tomography on the same needle-like sample reveals the NbO_2, Nb_2O_5, NbO, Nb stacking sequence; annular bright-field imaging is used to visualize directly hydrogen atoms in bulk β-NbH.
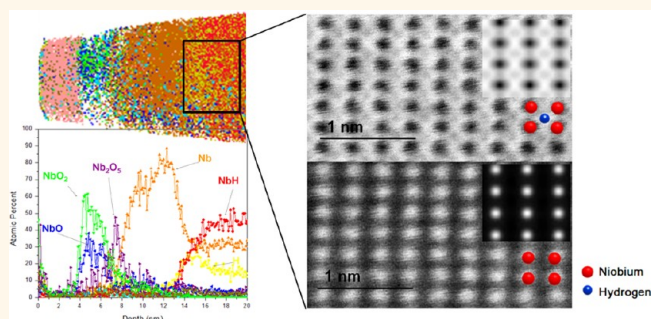
KEYWORDS: Nb · NbH · Nb oxides · atom-probe tomography · aberration-corrected STEM · annular bright-field images

Niobium is widely used in superconducting radio frequency (SRF) cavities for high-power linear accelerators.[1] Compared to a normal conducting material, such as copper, a great advantage of Nb cavities is the many orders of magnitude higher intrinsic quality factor (Q), due to extremely low power losses on the cavity wall.[2] Additionally, SRF cavities exhibit high accelerating electric-field gradients for operation in continuous-wave and long-pulse modes.[3] Therefore, such accelerators can be shorter and have less beam disruption, which dramatically benefits high-current applications. The performance of SRF cavities may, however, be limited by complex fabrication steps including forming, welding, and chemical and/or electrolytic polishing. During fabrication, small atoms, such as hydrogen and oxygen, reside as interstitial atoms in Nb bcc's structure and play significant roles in forming niobium oxides and niobium hydrides, which are believed to reduce the Q-factor.[4−6]

Hydrogen dissolves interstitially in Nb bcc's lattice structure. According to the Nb−H phase diagram, NbH, with a face-centered-orthorhombic (fco) structure, or NbH_2, with a face-centered-cubic (fcc) structure, forms depending on the H/Nb atomic concentration ratio.[7−9] Above room temperature, the β-phase (fco) with a H/Nb ratio from 0.7 to 1.1
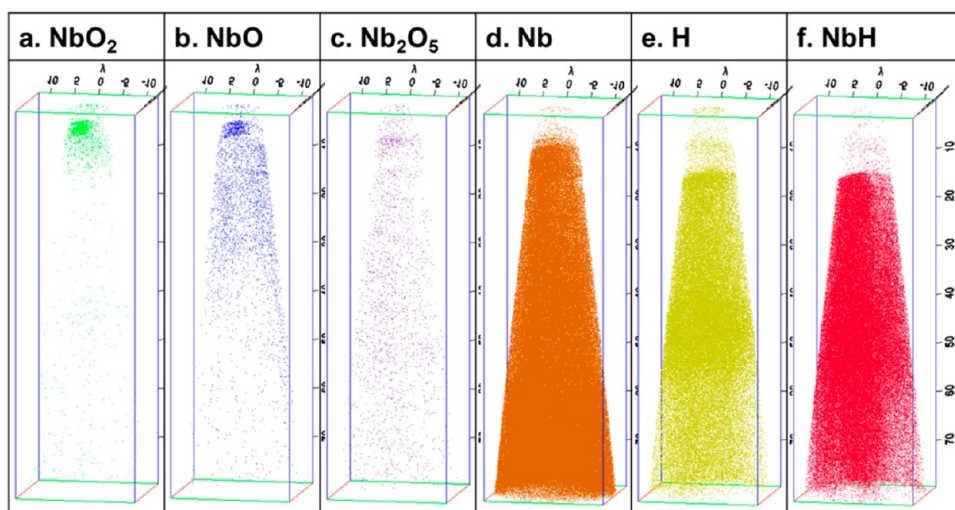
Figure 1. 3-D atom-probe tomographic reconstruction. Six different majority species are detected out of a total of 705 531 atoms collected, constituting a microtip, which are (a) NbO_2, (b) NbO, (c) Nb_2O_5, (d) Nb, (e) H, and (f) NbH. Three different types of niobium oxides are formed at the top-most surface of the SRF Nb material within ~5 nm in depth. Then, Nb, H, and NbH atoms are detected below the niobium oxide layer. Each dot represents a single atom, but not to scale. The unit for the sides of the rectangular parallelepiped is nm.

can form as a result of the ordering of H atoms in tetrahedral positions in an orthorhombic structure.[10,11] A pressure−composition isotherm for the Nb−H system (H_2 pressure *versus* H/Nb ratio) indicates a H/Nb ratio of the β-phase exhibiting a plateau in the H_2 pressure, ranging from 1.5 atm at 40 °C to 50 atm at 131 °C.[12] For temperatures less than 230 K, different ordered hydrides, such as ε (fco), ζ (fco), γ (pseudocubic), and λ (unconfirmed) form from the β-phase.[13]

Another interstitial element found in Nb SRF cavity material is oxygen. Oxygen atoms are located in octahedral sites in Nb (bcc).[14,15] Three different oxide phases, NbO, NbO_2, and Nb_2O_5, have been reported to form at the surface of pure Nb with thicknesses of less than 10 nm.[15−18] Since the penetration depth of the SRF cavity's electric field is ~50 nm, such oxide layers can be detrimental to the Bardeen−Cooper−Schrieffer surface resistance.[2] Using atom-probe tomography[16] and *in situ* X-ray investigations,[15] the surface niobium oxide was found to be mainly Nb_2O_5, while electron energy-loss spectroscopy (EELS) studies showed the presence of other Nb valence states [NbO (Nb^{2+}), NbO_2 (Nb^{4+}), and Nb_2O_5 (Nb^{5+})] in the surface oxide layer.[19,20]

While this complex interplay of different phases, impurities, and interfaces in Nb has been studied extensively, a detailed atomic-resolution characterization of the Nb oxide and hydride phases is still lacking, due to either the lack of spatial resolution or the inability to quantify interstitial hydrogen and oxygen while determining the atomic structure. Although several studies utilized atom-probe tomography together with STEM and EELS,[21−23] no direct observation results have been reported on H or O interstitial atoms. Herein, we present the first atomic-scale study to

combine picosecond ultraviolet laser-assisted local-electrode atom-probe (LEAP) tomography and a spherical aberration-corrected STEM imaging and EELS between 94 and 300 K on the same needle-like sample prepared by the focused ion-beam (FIB) method.

RESULTS AND DISCUSSION

Characterization in this article was performed at the atomic scale using a LEAP tomograph, which is a point-projection microscope, which relies on the principle of an enhanced electric field at the surface of a sharply pointed microtip, maintained at a high positive potential.[24−27] For sufficiently large applied voltages and a sharp microtip, the electric field at a tip's surface can produce field evaporation on an atom-by-atom and atomic layer-by-layer basis; individual evaporated ions are then accelerated away from the positively charged microtip's surface along trajectories that are orthogonal to the electric equipotentials. The time-of-flight (TOF) of each field-evaporated ion is detected and measured utilizing a 2-D position-sensitive detector. By combining the TOFs and the *x*-, *y*-, and *z*-positional information of all the atoms in an analyzed volume, a three-dimensional reconstruction of a volume of material is obtained with subnanoscale spatial resolution, Figure 1.

A total of 705 531 ions were detected during a LEAP tomographic experiment. Among the collected field-evaporated ions, six different atoms or compounds, H, Nb, NbH, NbO, NbO_2, and Nb_2O_5, were detected and analyzed based on their mass-to-charge state (*m/n*) ratios. Three-dimensional (3-D) reconstructions of the LEAP tomographic data are displayed in Figure 1. The minor species, O and Ga, are not displayed because of their small concentrations, both <5 at. %: Pt is not
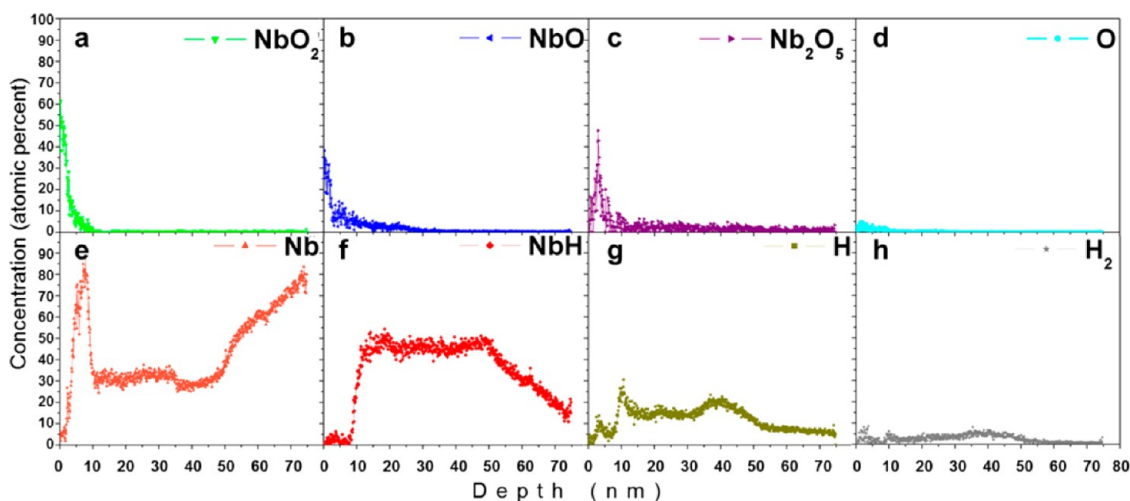
Figure 2. Depth concentration profiles. Quantitative concentration analyses of individual atoms based on a 3-D reconstruction of the microtip: (a) NbO_2, (b) NbO, (c) Nb_2O_5, (d) O, (e) Nb, (f) NbH, (g) H, (h) H_2.

displayed because it was intentionally deposited on the microtip to protect it from the radiation damage caused by Ga^+ ions. Figure 1 displays a discrete interface between the oxide layer, which consists of NbO_2 (Figure 1a), NbO (Figure 1b), and Nb_2O_5 (Figure 1c), and a Nb and H-enriched layer exhibiting Nb (Figure 1d), H (Figure 1e), and NbH (Figure 1f).

Quantitative information from the 3-D reconstruction is obtained by plotting atomic concentration *versus* depth profiles, Figure 2. Concentrations of NbO, NbO_2, Nb_2O_5, and O are found in the range from 0 to 10 nm in depth. NbO and NbO_2 exhibit maximum concentrations of ~40 and 55 at. %, respectively. Nb_2O_5 exhibits a maximum concentration of ~50 at. % at ~3 nm below the apex of the microtip. Below the oxide layer, a pure Nb layer of ~5 nm thickness is detected, followed by a relatively thick (~40 nm) NbH layer. It is worthwhile noting that we measured partial pressures of residual gases in the LEAP ultrahigh vacuum (UHV) chamber. The dominant partial pressures of residual gases are P_{H_2O} ~5.5 × 10^{-13} and P_{H_2} ~2.7 × 10^{-13} Torr. Therefore, residual H_2 gas inside the UHV chamber did not play a significant role in quantitative chemical analyses displayed in Figure 2. Figure 2 also demonstrates that LEAP tomography produces continuous and smooth field evaporation of the niobium subsurface region through the niobium oxide/niobium hydride/Nb interfaces. Since ultraviolet picosecond laser pulsing causes the thermal evaporation of ions from the surface of a microtip maintained at positive potential, it eliminates the periodically varying Maxwell elastic stresses[28] associated with pulsed electric-field evaporation, thereby reducing the susceptibility of a microtip to fracture.

The 2-D cross-sectional view of 3-D LEAP tomographic images exhibits crystallographic orientation information, poles, and zone lines. Figure 3 exhibits contrast caused by Nb and Nb oxides from the apex of

the microtip down to 5 nm in depth, Figure 3a, and Nb, NbO, H, and NbH from 15 to 30 nm, Figure 3b. These two depth ranges show clear niobium oxide and niobium hydride layers of the microtip. (Other depth ranges are available in the Supporting Information, Figure S1.) This is attributed to local electric-field variations associated with different crystallographic orientations on the surface of the microtip, which results in a smaller hit density of ions on the 2-D detector. On the basis of Figure 3, all niobium oxides and NbH are distributed around the [$\bar{1}$10] pole. Figure 3b, in particular, indicates that NbO is also enriched in the vicinity of the [001] and [100] poles, while NbH is depleted around these poles. NbH ions produce, however, 6-fold symmetry around the [$\bar{1}$10] pole. Each pole can be identified on the basis of the assumption that the field-desorption pattern is, to first order, a stereographic projection with the main [*hkl*] poles being indexed based on this assumption.

To confirm the presence of interstitial atoms, O and H, in pure Nb, more direct imaging was performed using STEM and EELS analysis in the probe aberration-corrected cold-field emission gun JEOL JEM-ARM200CF at the University of Illinois at Chicago (UIC). At a 200 kV primary electron energy, the JEM-ARM200CF provides a spatial resolution of better than 78 pm for high-angle annular dark-field (HAADF) and simultaneous annular bright-field (ABF) imaging (Supporting Information, Figure S2). For atomic-resolution EELS, an energy resolution of 0.35 eV can be achieved. A Gatan LN_2 double-tilt sample stage permits *in situ* cooling experiments in the temperature range between 94 and 300 K.

Figure 4a shows an atomic resolution HAADF image of a Nb grain in the [110] orientation at the SRF's cavity surface. This image contains the Pt protective layer, which was intentionally created during FIB sample preparation to reduce Ga^+ ion-implantation damage.
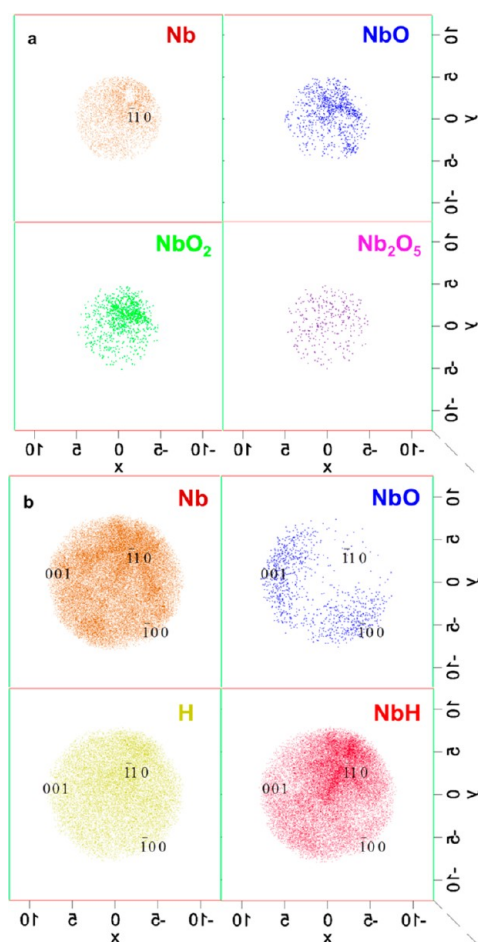
Figure 3. Cross-sectional top views of 3-D reconstructed image displayed in Figure 1. (a) Top views of Nb, NbO, NbO$_2$, and Nb$_2$O$_5$ from the apex of the microtip down to 5 nm. Three types of niobium oxide are enriched around the [$\bar{1}$10] pole of Nb. (b) Top views of Nb, NbO, H, and NbH from 15 to 30 nm of the microtip. NbO is distributed around the [001] and [$\bar{1}$00] poles of Nb. Alternatively, H and NbH are enriched around the [$\bar{1}$10] pole of Nb. Indexing of the [*hkl*] poles is based on a stereographic projection. Each dot represents a single atom, but not to scale. The unit for the sides of the rectangular parallelepiped is nm.

An amorphous layer is observed between the Pt protective layer and the bulk Nb grain, which was identified as the surface oxide previously measured by LEAP tomography. In agreement with the LEAP tomographic results, we find the entire oxide thickness to be ~5 nm.

The local composition of the amorphous oxide layer can be identified using either core-loss or low-loss EELS spectra. Due to the small thickness of the surface oxide layer and the concomitant small signal of the O K- or Nb M-edge core-loss peaks, we focus our analysis on the low-loss features. Previously, Bach *et al.*[20] have demonstrated that changes in the plasma peaks can be used to distinguish between different types of Nb oxides. More specifically, the low-loss peaks in the energy range between 5 and 50 eV exhibit unique triple-peak features,[29] depending on the oxide type, NbO, NbO$_2$, or Nb$_2$O$_5$. Figure 4b demonstrates clearly that the composition of the 5 nm thick layer changes from

predominantly NbO$_2$ for the top 2 nm to Nb$_2$O$_5$ coexisting with other oxide types, such as NbO$_2$ for the next 2 nm. Approaching the Nb interface, a 1 nm thick NbO layer is detected, which extends into the Nb grain for 2–3 nm; see areas 7 and 8 in Figure 4a.

To further quantify the phase of the hydride present in the Nb grain at room temperature and at 94 K, we performed selective area diffraction (SAD) analyses of the grain displayed in Figure 4a. Figure 5a shows the SAD pattern of Nb [110] at room temperature with the major spots labeled according to the bcc structure. Figure 5b displays a SAD pattern, which shows the major spots of pure Nb [110] along with weak spots in between the bright Nb spots. These weak spots are from the interstitial H superlattice and are consistent with the β-NbH phase. When the sample temperature is reduced to 94 K, using a double-tilt LN$_2$ cooling stage, a different configuration of superlattice spots emerges next to the β-phase region as shown in Figure 5c. This phase is identified as the ζ-phase, a transition phase from β- to ε-phase, or *vice versa*, based on a crystallographic orientation relationship (space group symmetry reported as *C*222),[8,9] with a formation temperature higher than 94 K, as indicated in the Nb–H binary phase diagram.[30]

Although the SAD patterns indicate the presence of an ordered β-NbH phase, the HAADF image shown in Figure 4a does not exhibit any sign of H atomic columns, due to the low scattering amplitude of H compared to Nb. More specifically, since the image intensity in HAADF imaging is proportional to approximately Z^2, the intensity of the Nb atomic columns ($Z = 41$) will overwhelm the signal of the H atomic columns,[31−33] even with a 68 pm electron probe. Direct imaging of H atomic columns in a crystal lattice is, however, now possible by using ABF imaging.[34,35] ABF imaging, which uses the bright-field signal of the transmitted electron beam, but excludes the first 11 mrad of the bright-field disk, provides improved contrast for light elements, specifically H,[34,35] N, O,[36] or C. Most importantly, by using aberration-corrected STEM imaging, the focus for both HAADF and ABF is very similar, so that simultaneous imaging using HAADF and ABF is now possible.

Figure 6a shows the atomic-resolution ABF and HAADF images of β-NbH, with the H atomic columns clearly visible in the interstitial positions in only the ABF image. The HAADF image shows the bright spots for the Nb atomic columns in the [110] orientation. Using multislice image calculations (Supporting Information, Figure S3) for a range of sample thicknesses, we confirm that the interstitial signal is indeed due to H atomic columns and not due to imaging artifacts (*e.g.*, probe tails or higher order aberrations) or other light elements, such as O or C. In fact, the thickness of the NbH crystal was determined using our image calculations (Supporting Information, Figure S4) to be
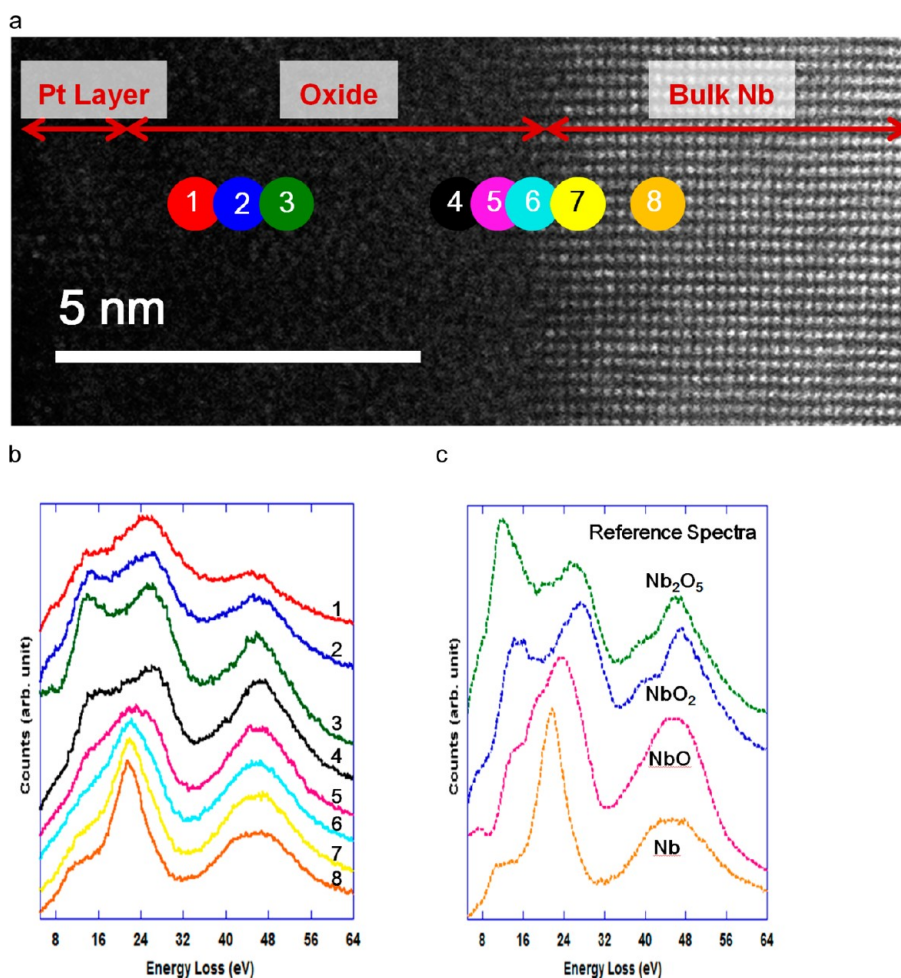
Figure 4. HAADF STEM image and EELS low-loss peak of oxide and suboxide layers. (a) Atomic-resolution HAADF-contrast image of a Nb grain in the [110] orientation at the SRF cavity surface. The amorphous oxide layer including NbO_2, NbO, and Nb_2O_5 is seen between the Pt layer and bulk Nb, and its thickness is between 3 and 5 nm. (b) Experimental EELS spectra taken from the colored spots indicated in (a). (c) EELS spectra taken from standard powder samples for different oxidation states of Nb. It can be seen that NbO_2 is the topmost oxide, which is followed by Nb_2O_5 and NbO. NbO and Nb coexist in the subsurface region of bulk Nb, as seen in the yellow and orange spectra, respectively.
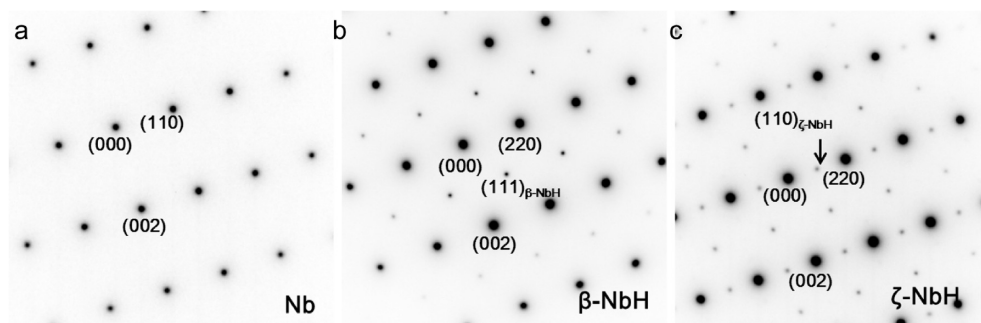

Figure 5. SAD patterns taken from different locations within a single Nb [110] grain. (a) SAD pattern taken from an area similar to that shown in Figure 4a at room temperature. The pattern shows a typical [110]-type zone of the bcc Nb structure. (b) SAD pattern taken from an adjacent area showing superlattice reflections between bright bcc spots. This pattern is identified as that of the face-centered-orthorhombic β-NbH phase. (c) SAD pattern at 94 K from the same area shown in (b), indicating that some of the β-NbH phase has undergone a transformation to the ζ-NbH (face-centered-orthorhombic) phase.

between 8 and 10 nm, which matches that reported by Ishikawa *et al.*[37]

Additional proof for the presence of NbH is provided by our EELS analysis (Figure 6b), which displays an additional low-loss peak in the energy range between 5 and 7 eV. This peak in the EELS spectra is visible only in the area that shows the superlattice in the SAD or the interstitial H-columns in the ABF image. This peak is
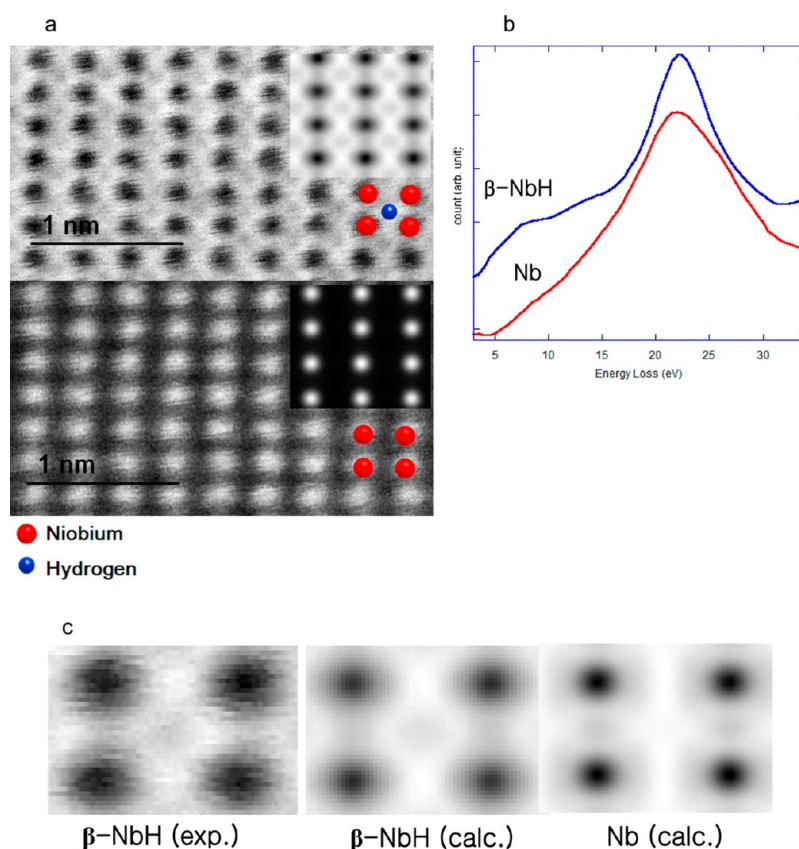
Figure 6. Direct observation of hydrogen atoms near niobium oxide/bulk-Nb interface area using the ABF detector and the corresponding EELS H K-edge. (a) Unprocessed ABF and HAADF images of β-NbH [110] at room temperature. The ABF image shows clearly the atomic columns of both Nb and H atoms. A calculated ABF image of β-NbH [110] is displayed as an inset, matching the experimentally measured contrast. The H atomic columns are not visible in the HAADF image or the calculated image. (b) EELS spectrum taken from the region shown, which clearly displays a H K-edge signal at 8 eV. (c) Average images of one unit cell of β-NbH [110], comparing the experimental image contrast to that obtained by multislice calculations for β-NbH [110] and pure Nb [110].

attributed to the H K-edge, as reported for VH_2[38] and YH_2.[37] Additionally, we observe a small shift of the large peak located at 22 eV in bulk Nb. This peak is shifted by 0.8 eV toward higher energies for the areas that exhibit the extra H peak.

Figure 6c displays an averaged image of one unit cell of NbH [110], as well as the calculated image for β-NbH [110] and pure Nb [110] for a sample thickness of 8 nm. This comparison demonstrates that the interstitial intensity measured in the ABF images is indeed due to the presence of H atomic columns, since pure Nb does not show any interstitial intensity, while other light elements, such as C or O, exhibit a significantly higher intensity than measured in the experimental image (Supporting Information, Figure S4). It is interesting to note that the contrast of the H atomic columns appears to be visible only for samples thinner than 12 nm, while for thicker samples the H atomic column contrast is again too weak, even in ABF imaging. Therefore, direct characterization of NbH phases using ABF imaging appears only possible for very thin sections of the atom-probe tomograph microtip and imposes an additional restriction on the sample preparation using a dual-beam focused ion-beam microscope.

CONCLUSIONS

In summary, we have demonstrated, for the first time, that atomic-scale three-dimensional characterization of complex structures, including amorphous/crystalline interfaces, is possible by combining laser-assisted LEAP tomography and aberration-corrected STEM imaging and spectroscopy on the same needle-like samples prepared by FIB microscopy. While LEAP tomography permits three-dimensional atom-by-atom reconstruction of ultrathin layers and provides a high sensitivity to elements, such as H at 25 K, atomic-resolution STEM imaging and EELS enable atomic- and electronic-structure characterization of a two-dimensional projected structure, in the temperature range between 94 and 300 K. By using both techniques sequentially on the same needle-like sample, we have characterized the evolution of Nb oxide and Nb hydride phases over a large temperature range. We find remarkable agreement between the stacking sequence of the 5 nm thick Nb oxide surface layer determined by LEAP tomography and EELS as NbO_2, Nb_2O_5, and NbO on top of metallic Nb. Below the surface of Nb grains, we find an ~40 nm thick region with a high concentration of H, which in some areas

forms an ordered β-NbH phase at room temperature. At 94 K or below we report the presence of multiple phases of NbH, including ζ and β. Identifying the exact niobium oxide stacking sequence on the Nb surface, as well as the presence of Nb hydride phases in bulk Nb grains, as shown herein, will be of tremendous value to the SRF community, since it will enable the tailoring of specific pinning centers and reduction of surface losses during the cavity production process. Moreover, the combination of methods described herein is not limited to Nb SRF-cavity materials only. On the contrary, the combination of laser-assisted LEAP tomography and aberration-corrected STEM imaging and spectroscopy on the same sample structure can now be used to determine the three-dimensional atomic and electronic structures of semiconductor quantum dots, amorphous intergranular ceramic films, or other complex metallic structures.

METHODS

A pure Nb sample (residual resistivity ratio > 300), with the approximate dimensions $25 \times 25 \times 2$ mm^3, was very kindly supplied by Dr. Alex Romanenko of Fermi National Accelerator Laboratory (FNAL), Batavia, IL, USA. The coupons were cut from a single-crystal Nb sheet using electrical discharge machining. To simulate SRF cavity conditions, specific surface finishes, such as buffered chemical polishing and electropolishing, were utilized.[39]

An ultrahigh vacuum, with a total pressure range of $(2-3) \times 10^{-11}$ Torr, ultraviolet laser-assisted LEAP (LEAP 4000XSi, Cameca, Madison, WI, USA) tomograph was employed at Northwestern University, utilizing picosecond laser pulses with a wavelength of 355 nm, an evaporation rate (ion pulse^{-1}) of 0.50%, a pulse repetition rate of 250 kHz, and an energy pulse^{-1} of 50 pJ. Partial pressures of residual gases including H$_2$ in UHV were monitored using a residual gas analyzer (Transpector 2, Inficon, East Syracus, NY, USA). LEAP tomographic specimens were prepared using a dual-beam focused-ion beam microscope (Helios Nanolab., FEI Co., Hillsboro, OR, USA) with 30 kV Ga$^+$, followed by 5 kV Ga$^+$ and 2 kV Ga$^+$ to decrease the Ga$^+$ ion contamination. To prevent radiation damage produced by Ga$^+$ ions during FIB nanomachining, a 150 nm thick Pt protective layer was deposited onto the surface of the Nb coupons using an ion-beam sputter deposition system (SBT-IBS, South Bay Technology, San Clemente, CA, USA). Needle-shaped specimens with a microtip radius of $\sim$20 nm were fabricated using the FIB-based lift-out method and attached to Si microposts on a coupon.[40] The coupon was subsequently inserted into the LEAP tomograph's UHV chamber and cooled to 30 K prior to performing pulsed laser-assisted evaporation analyses. The microtips were maintained at a positive potential, while the evaporation of ions was triggered by the picosecond UV laser pulses. The times-of-flight of the detected ions were used to produce three-dimensional reconstructions using IVAS software (version 3.6.1).

All high-angle annular dark-field and annular bright-field images as well as electron energy-loss spectra shown in this study were acquired using the probe aberration-corrected JEOL JEM-ARM200CF at UIC, equipped with a 200 kV cold-field emission gun, postcolumn Gatan Enfina EELS spectrometer, and HAADF and ABF detectors. A 22 mrad probe convergence semiangle is used for HAADF and ABF imaging as well as electron energy-loss spectroscopy. The detector inner angle for HAADF is 90 mrad, while the detector range for ABF imaging is 11–22 mrad. A collection semiangle of 45 mrad for EELS was used in the experiments. The *in situ* cooling experiments were conducted using a Gatan 636 LN$_2$ double-tilt cooling stage, which can be operated in the temperature range between 94 and 300 K. A thin foil was prepared using a conventional lift-out and ion-beam milling technique, employing a dual-beam FIB microscope described elsewhere.[41−43]

Conflict of Interest: The authors declare no competing financial interest.

Supporting Information Available: APT images with various depth ranges, special resolution of HRSTEM using FFT of HAADF image, electron-probe shape used in multislice calculation for ABF images, and resulting intensity profiles. This material is available free of charge *via* the Internet at http://pubs.acs.org.

REFERENCES AND NOTES

1. Phinney, N.; Toge, N.; Walker, N. *International Linear Collider Reference Design Report*, Vol III-Accelerator; CERN — European Laboratory for Particle Physics: Geneva, Switzerland, 2007; Vol. 3.
2. Padamsee, H. *RF Superconductivity: Science, Technology, and Applications*; Wiley-VCH: Weinheim, 2009.
3. Ge, M.; Wu, G.; Burk, D.; Ozelis, J.; Harms, E.; Sergatskov, D.; Hicks, D.; Cooley, L. D. Routine Characterization of 3D Profiles of SRF Cavity Defects Using Replica Techniques. *Supercond. Sci. Technol.* **2011**, *24*, 035002.
4. Romanenko, A.; Padamsee, H. The Role of Near-Surface Dislocations in the High Magnetic Field Performance of Superconducting Niobium Cavities. *Supercond. Sci. Technol.* **2010**, *23*, 045008.
5. Ricker, R. E.; Myneni, G. R. Evaluation of the Propensity of Niobium to Absorb Hydrogen During Fabrication of Superconducting Radio Frequency Cavities for Particle Accelerators. *J. Res. Natl. Inst. Stan.* **2010**, *115*, 353–371.
6. Isagawa, S. Influence of Hydrogen on Superconducting Niobium Cavities. *J. Appl. Phys.* **1980**, *51*, 6010–6017.
7. Schober, T. Niobium-Hydrogen System - Electron-Microscope Study 0.1. Room-Temperature Results. *Phys. Status Solidi A* **1975**, *29*, 395–406.
8. Schober, T. Niobium-Hydrogen System - Electron-Microscope Study 0.2. Low-Temperature Structures. *Phys. Status Solidi A* **1975**, *30*, 107–116.
9. Hauck, J. Structural Relations between Vanadium, Niobium, Tantalum Hydrides and Deuterides. *Acta Crystallogr. A* **1978**, *34*, 389–399.
10. Gabriel, S. B.; Silva, G.; Candioto, K. C. G.; Santos, I. D.; Suzuki, P. A.; Nunes, C. A. Niobium Hydrogenation Process Effect of Temperature and Cooling Rate from the Hydrogenation Temperature. *Int. J. Refract. Met. H* **2011**, *29*, 134–137.
11. Schober, T.; Wenzl, H. Beta-Phase Melting and Solidification Phenomena in Niobium-Hydrogen System. *Phys. Status Solidi A* **1976**, *33*, 673–681.

12. Reilly, J. J.; Wiswall, R. H. Higher Hydrides of Vanadium and Niobium. *Inorg. Chem.* **1970**, *9*, 1678–1682.

13. Makenas, B. J.; Birnbaum, H. K. Phase-Changes in the Niobium Hydrogen System 2. Low-Temperature Hydride Phase-Transitions. *Acta Metall. Mater.* **1982**, *30*, 469–481.

14. Baker, C.; Birnbaum, H. K. Anelastic Studies of Hydrogen Diffusion in Niobium. *Acta Metall. Mater.* **1973**, *21*, 865–872.

15. Delheusy, M.; Stierle, A.; Kasper, N.; Kurta, R. P.; Vlad, A.; Dosch, H.; Antoine, C.; Resta, A.; Lundgren, E.; Andersen, J. X-ray Investigation of Subsurface Interstitial Oxygen at Nb/Oxide Interfaces. *Appl. Phys. Lett.* **2008**, *92*, 101911.

16. Yoon, K. E.; Seidman, D. N.; Antoine, C.; Bauer, P. Atomic-Scale Chemical Analyses of Niobium Oxide/Niobium Interfaces *via* Atom-Probe Tomography. *Appl. Phys. Lett.* **2008**, *93*, 132502.

17. Yoon, K. E.; Seidman, D. N.; Bauer, P.; Boffo, C.; Antoine, C. Atomic-Scale Chemical-Analyses of Niobium for Superconducting Radio-Frequency Cavities. *IEEE Trans. Appl. Supercond.* **2007**, *17*, 1314–1317.

18. Sebastian, J. T.; Seidman, D. N.; Yoon, K. E.; Bauer, P.; Reid, T.; Boffo, C.; Norem, J. Atom-Probe Tomography Analyses of Niobium Superconducting RF Cavity Materials. *Physica C* **2006**, *441*, 70–74.

19. Tao, R. Z.; Todorovic, R.; Liu, J. J.; Meyer, R. J.; Arnold, A.; Walkosz, W.; Zapol, P.; Romanenko, A.; Cooley, L. D.; Klie, R. F. Electron Energy-Loss Spectroscopy Study of Metallic Nb and Nb Oxides. *J. Appl. Phys.* **2011**, *110*, 124313.

20. Bach, D.; Schneider, R.; Gerthsen, D. EELS of Niobium and Stoichiometric Niobium-Oxide Phases—Part II: Quantification. *Microsc. Microanal.* **2009**, *15*, 524–538.

21. Devaraj, A.; Nag, S.; Srinivasan, R.; Williams, R. E. A.; Banerjee, S.; Banerjee, R.; Fraser, H. L. Experimental Evidence of Concurrent Compositional and Structural Instabilities Leading to Omega Precipitation in Titanium-Molybdenum Alloys. *Acta Mater.* **2012**, *60*, 596–609.

22. Thompson, G. B.; Genc, A.; Morris, R.; Torres, K. L.; Fraser, H. L. Correlation Between TEM Imaging and Microanalysis for Atom Probe Reconstruction Verification. *Microsc. Microanal.* **2009**, *15*, 250–251.

23. Srinivasan, R.; Banerjee, R.; Hwang, J. Y.; Viswanathan, G. B.; Tiley, J.; Dimiduk, D. M.; Fraser, H. L. Atomic Scale Structure and Chemical Composition across Order-Disorder Interfaces. *Phys. Rev. Lett.* **2009**, *102*, 086101.

24. Miller, M. K. *Atom Probe Tomography: Analysis at the Atomic Level*; Kluwer Academic/Plenum Publishers: New York, 2000.

25. Cerezo, A.; Godfrey, T. J.; Sijbrandij, S. J.; Smith, G. D. W.; Warren, P. J. Performance of an Energy-Compensated Three-Dimensional Atom Probe. *Rev. Sci. Instrum.* **1998**, *69*, 49–58.

26. Seidman, D. N. Three-Dimensional Atom-Probe Tomography: Advances and Applications. *Annu. Rev. Mater. Res.* **2007**, *37*, 127–158.

27. Seidman, D. N.; Stiller, K. An Atom-Probe Tomography Primer. *MRS Bull.* **2009**, *34*, 717–724.

28. Panofsky, W. K. H.; Phillips, M. *Classical Electricity and Magnetism*, 2nd ed.; Dover Publications: Mineola, NY, 2005.

29. Bach, D.; Schneider, R.; Gerthsen, D.; Verbeeck, J.; Sigle, W. EELS of Niobium and Stoichiometric Niobium-Oxide Phases—Part I: Plasmon and Near-Edges Fine Structure. *Microsc. Microanal.* **2009**, *15*, 505–523.

30. Schober, T.; Wenzl, H. The Systems NbH(D), TaH(D), VH(D): Structures, Phase Diagrams, Morphologies, Methods of Preparation, Hydrogen in Metals II. Alefeld, G.; Völkl, J., Eds.; Springer: Berlin, 1978; Vol. 29, pp 11−71.

31. Crewe, A. V. Chapter 1. The Work of Albert Victor Crewe on the Scanning Transmission Electron Microscope and Related Topics. In *Advances in Imaging and Electron Physics*, Peter, W. H., Ed.; Elsevier, 2009; Vol. 159, pp 1−61.

32. Pennycook, S. J.; Boatner, L. A. Chemically Sensitive Structure-Imaging with a Scanning Transmission Electron Microscope. *Nature* **1988**, *336*, 565–567.

33. Pennycook, S. J. Z-Contrast STEM for Materials Science. *Ultramicroscopy* **1989**, *30*, 58–69.

34. Findlay, S. D.; Shibata, N.; Sawada, H.; Okunishi, E.; Kondo, Y.; Ikuhara, Y. Dynamics of Annular Bright Field Imaging in Scanning Transmission Electron Microscopy. *Ultramicroscopy* **2010**, *110*, 903–923.

35. Okunishi, E.; Ishikawa, I.; Sawada, H.; Hosokawa, F.; Hori, M.; Kondo, Y. Visualization of Light Elements at Ultrahigh Resolution by STEM Annular Bright Field Microscopy. *Microsc. Microanal.* **2009**, *15*, 164–165.

36. Klie, R. F.; Qiao, Q.; Paulauskas, T.; Ramasse, Q.; Oxley, M. P.; Idrobo, J. C. Examining the Structure and Bonding in Complex Oxides Using Aberration-Corrected Imaging and Spectroscopy. *Phys. Rev. B* **2012**, *85*, 054106.

37. Ishikawa, R.; Okunishi, E.; Sawada, H.; Kondo, Y.; Hosokawa, F.; Abe, E. Direct Imaging of Hydrogen-Atom Columns in a Crystal by Annular Bright-Field Electron Microscopy. *Nat. Mater.* **2011**, *10*, 278–281.

38. Findlay, S. D.; Saito, T.; Shibata, N.; Sato, Y.; Matsuda, J.; Asano, K.; Akiba, E.; Hirayama, T.; Ikuhara, Y. Direct Imaging of Hydrogen within a Crystalline Environment. *Appl. Phys. Express* **2010**, *3*, 116603.

39. Cooley, L. D.; Burk, D.; Cooper, C.; Dhanaraj, N.; Foley, M.; Ford, D.; Gould, K.; Hicks, D.; Novitski, R.; Romanenko, A.; *et al.* Impact of Forming, Welding, and Electropolishing on Pitting and the Surface Finish of SRF Cavity Niobium. *IEEE Trans. Appl. Supercond.* **2011**, *21*, 2609–2614.

40. Miller, M. K.; Russell, K. F.; Thompson, K.; Alvis, R.; Larson, D. J. Review of Atom Probe FIB-Based Specimen Preparation Methods. *Microsc. Microanal.* **2007**, *13*, 428–436.

41. Giannuzzi, L. A.; Stevie, F. A. A Review of Focused Ion Beam Milling Techniques for TEM Specimen Preparation. *Micron* **1999**, *30*, 197–204.

42. Li, J.; Malis, T.; Dionne, S. Recent Advances in FIB-TEM Specimen Preparation Techniques. *Mater. Charact.* **2006**, *57*, 64–70.

43. Giannuzzi, L. A.; Stevie, F. A. *Introduction to Focused Ion Beams: Instrumentation, Theory, Techniques, and Practice*; Springer: New York, 2005.